International Journal of Multiphase Flow 47 (2012) 25–36

Contents lists available at SciVerse ScienceDirect

International Journal of Multiphase Flow

journal homepage: www.elsevier.com/locate/ijmulflow

Direct simulations of dense suspensions of non-spherical particles

Orest Shardt *, J.J. Derksen

Department of Chemical and Materials Engineering, University of Alberta, Edmonton, Alberta, Canada

ARTICLE INFO

Article history:
Received 17 March 2012
Received in revised form 29 May 2012
Accepted 4 June 2012
Available online 21 June 2012

Keywords:
Non-spherical particle
Sedimentation
Dense suspension
Lattice Boltzmann method
Immersed boundary
Erythrocyte

ABSTRACT

We describe a method for the direct simulation of high-solids-volume-fraction (up to 45%) suspensions of non-spherical rigid particles that are non-colloidal and slightly denser than the interstitial fluid. The lattice-Boltzmann method is used to solve for the flow of the interstitial Newtonian fluid, and the immersed boundary method is used to enforce a no-slip boundary condition at the surface of each particle. The surface points for the immersed boundary method are also employed for collision handling by applying repulsive forces between the surface points of nearby particles. We also discuss methods for integrating the equations of particle motion at low density ratios and propose a method with improved accuracy. The methods are used to simulate rigid particles shaped like red blood cells. We report on the effect of the solids volume fraction on the sedimentation rate using a Richardson–Zaki model, and we describe the orientation of the particles during sedimentation. The particles settle in a preferentially vertical orientation at terminal particle Reynolds numbers near one. We compare a simulation at a 35% solids volume fraction with typical erythrocyte sedimentation rates, a common blood test. We find an order of magnitude lower sedimentation rate than the value for healthy adults. The discrepancy is attributed to the omission of agglomeration-inducing inter-cellular forces and the treatment of the red blood cells as rigid particles in the simulations.

1. Introduction

Recent research has studied the behavior of dense suspensions of sedimenting or fluidized spheres. For example, planar instabilities during fluidization were simulated by Derksen and Sundaresan (2007). Sedimentation of spheres in non-Newtonian fluids has also been studied (Derksen and Shardt, 2010). Since real particles are often non-spherical, it is interesting to study the impact of the particle shape on the flow behavior of dense suspensions. For example, slender rods assume a preferential orientation as they sediment (Herzhaft et al., 1996).

Literature on the sedimentation and fluidization of non-spherical particles is not common. Richardson and Zaki (1954) presented data for high Reynolds number sedimentation of disks and other shapes in turbulent flow ($Re > 2000$). Recently, Fonseca and Herrmann (2004) simulated oblate ellipsoids at Reynolds numbers of 0.04 and 7 with solids volume fractions up to 20%. He et al. (2010) presented experimental data for sedimenting disks of colloidal size (size at which Brownian motion becomes important) at $Re \approx 10^{-7}$ with solids volume fractions up to 20%. Whalley and Mullins (1992) studied orientation effects in colloidal clay disks undergoing centrifugation. We simulate non-colloidal non-spherical particles shaped as red blood cells (RBCs) sedimenting at Reynolds numbers around one and high solids volume fractions (30–45%).

Simulations of non-spherical particles could be applied to various systems. Simulations of RBC sedimentation could provide insight into the rheology and settling behavior of blood and allow for comparison with data from erythrocyte sedimentation rate (ESR) diagnostic tests. In industrial applications, fluidized or sedimenting particles are rarely spherical, but simulations commonly use spherical particles for simplicity. This simplification is also used to study erosion in rivers and sea beds, crystallization processes, and slurry pipeline transport. The sedimentation of non-spherical particles is also relevant to the design of drilling muds in the petroleum industry (Whalley and Mullins, 1992; Peden and Luo, 1987). Simulations of non-spherical particles would allow the effects of non-sphericity to be studied in these systems.

An important challenge in simulations of non-spherical particles (specifically in dense suspensions) is the efficient handling of collisions. In the immersed boundary method for imposing a no-slip boundary condition at the surface of each particle, evenly distributed surface points are required. In this paper, we use these points to handle collisions; we define repulsive forces between surface points for overlap prevention and momentum exchange.

This paper is organized as follows: We first describe the flow solver, the stability and accuracy of particle motion integration methods at low density ratios, and the forcing scheme for collision handling. Next, we describe benchmark simulations of single

* Corresponding author.
E-mail addresses: shardt@ualberta.ca (O. Shardt), jos@ualberta.ca (J.J. Derksen).

0301-9322/$ - see front matter © 2012 Elsevier Ltd. All rights reserved.
http://dx.doi.org/10.1016/j.ijmultiphaseflow.2012.06.007

particles. We then study dense suspensions and the effect of the solids volume fraction on the settling rate. We also investigate the orientation of the particles in the settling suspension. We then briefly compare a simulation with data for human blood and provide concluding remarks.

2. Simulation methods

2.1. Fluid flow and boundary conditions

As in previous simulations of the sedimentation of dense suspensions of solid spheres (ten Cate et al., 2002; Derksen and Sundaresan, 2007), we use the lattice Boltzmann method to solve for the flow of the fluid. The specific scheme employed is that of Somers (1993). It uses a regular cubic lattice, whose spacing is used as the length unit. We also take the time interval of a time step to be one. These reference scales define lattice units (l.u.) that are used for specifying quantities in the simulations. The domain is fully periodic, and a body force is applied to ensure that the forces acting on the domain are balanced (Derksen and Sundaresan, 2007). The no-slip boundary condition at the surface of each particle is enforced by using an immersed boundary method (Goldstein et al., 1993). With this method, body forces are applied to the fluid at the lattice nodes adjacent to uniformly distributed Lagrangian tracking points on the surface of each particle. These body forces cause the fluid velocity to match the velocity of the particle surface. The body forces can also be used to calculate the forces and torques acting on the solid particles, as described in Section 2.2. However, the inside of each particle contains fluid, and the effect of the force on the internal fluid mass and particle mass must be considered. This will be described in Section 2.2.1.

To simulate non-spherical particles using the immersed boundary method, we use surface points that are distributed uniformly over the surface of the particles. For spheres, explicit formulae are available to transform a pair of uniform random numbers each from the interval $[0,1]$ to points on the surface of a sphere (Arndt, 2008). For an arbitrary surface, the probability of placing a point in any region must be the fraction of the total area in that region. In this work, we consider axially symmetric non-spherical particles generated by the revolution of the profile $z(r)$ about the z-axis, where r is the radial distance from the z-axis. We employ a numerical adaptation of the method described by Arndt (2008) to randomly distribute the surface points. For each surface point, we obtain its angular position θ as a random number from $[0,2\pi]$. The probability distribution of the radial position $r \in [0,R]$ is

$$P(0 < r < r_0) = \frac{1}{A}\int_0^{r_0} dA \tag{1}$$

for all $r_0 \in [0,R]$, where A is the surface area of the particle, and R is the radius. The integral was evaluated numerically to obtain the probability of selecting a radial distance r from a finite number of subintervals of $[0,R]$. The method was used to place 3509 surface points (four points per square of width equal to one lattice spacing) on the surface of a red blood cell described using $z(r)$ according to Evans and Fung (1972), see Eq. (31), with a radius $R = 10$ l.u. and the other parameters scaled accordingly. Surface points were rejected if they were closer than 0.3 to another surface point to ensure satisfactorily even spacing between the points. The surface points and the surface outward normal vectors at these points are shown in Fig. 1. This reference set of surface point positions is stored in memory. In each time step of the simulation algorithm, the locations of the surface points for each particle are determined by transforming the reference points after the unit quaternion specifying the orientation of each particle has been updated (as described in Section 2.2.2). To speed up the rotational component of this affine transformation, quaternion multiplication is not used; instead, the rotation matrix is determined using Eq. (10), and matrix multiplication is used to rotate each surface point from the reference position. The gain in speed arises from the fact that only one computation of the rotation matrix is required for the 3509 surface points and 3509 normals on each particle.

2.2. Particle motion

We consider the motion of rigid particles each of which occupies a volume V and has a surface $S = \partial V$ inside a fluid.

2.2.1. Linear motion

The translational motion of a solid particle in a fluid is governed by the momentum balance (Feng and Michaelides, 2009)

$$\rho_s V\frac{\mathrm{d}\vec{v}}{\mathrm{d}t} = \oint_S \vec{\tau} dS + \left(\rho_s - \rho_f\right)V\vec{g} \tag{2}$$

where $\vec{v}$ is the velocity of the centre of mass, $\vec{g}$ is the gravitational acceleration, and ρ is the density. The subscript "s" denotes solid; "f" denotes fluid. Numerical evaluation of the traction $\vec{\tau}$ can be eliminated by considering the momentum balance for the internal fluid (Feng and Michaelides, 2009):

$$\oint_S \vec{\tau} dS = \int_V \vec{f} dV + \rho_f V\frac{\mathrm{d}\vec{v}}{\mathrm{d}t} \tag{3}$$

Here $\vec{f}$ is the external force acting on the particle and internal fluid, and in this case it is due to the immersed boundary method. Since the effect of applying forces to the internal fluid of the particle is generally small (Feng and Michaelides, 2009), the volume integral reduces to being an integral over the volume of a thin shell near the surface because the force is zero in the interior. Substitution of Eq. (3) into Eq. (2) provides the equation for the velocity of each particle:

$$\left(\rho_s - \rho_f\right)V\frac{\mathrm{d}\vec{v}}{\mathrm{d}t} = \int_V \vec{f} dV + \left(\rho_s - \rho_f\right)V\vec{g} \tag{4}$$

The numerical integration of this equation is described in Section 2.2.4. For the split-derivative integration methods that will be described, it is convenient to leave the difference on the left in an expanded form (as in Feng and Michaelides (2009)) and simplify to obtain:

$$\gamma\frac{\mathrm{d}\vec{v}}{\mathrm{d}t} - \frac{\mathrm{d}\vec{v}}{\mathrm{d}t} = \frac{1}{\rho_f V}\int_V \vec{f} dV + (\gamma - 1)\vec{g} \tag{5}$$

where γ is the density ratio ρ_s/ρ_f.

2.2.2. Rotational motion

The rotational motion of a particle is governed by

$$I\frac{\mathrm{d}\vec{\omega}}{\mathrm{d}t} = \vec{M} - \vec{\omega}\times(I\vec{\omega}) \tag{6}$$

where the angular velocity $\vec{\omega}$ and applied torque $\vec{M}$ are relative to a body-fixed reference frame. The inertia tensor I is constant and diagonal since the axes of the body-fixed coordinate system are chosen to match the principal axes of the particle. An analysis that is similar to the analysis for linear motion can be used to obtain the equation governing the angular velocity of each particle (Feng and Michaelides, 2009):

$$\rho_s I\frac{\mathrm{d}\vec{\omega}}{\mathrm{d}t} - \rho_f I\frac{\mathrm{d}\vec{\omega}}{\mathrm{d}t} = \rho_s \mathbf{S}^{-1}\int_V (\vec{x} - \vec{x}_c)\times\vec{f} dV - \left(\rho_s - \rho_f\right)\vec{\omega}\times(I\vec{\omega}) \tag{7}$$

Since the force $\vec{f}$ and $(\vec{x} - \vec{x}_c)$, where $\vec{x}_c$ is the position of the centre of mass, are in the lattice reference frame, the inverse of the rotation matrix $\mathbf{S}$, which is the transpose of $\mathbf{S}$, is required to transform the torque into body-fixed coordinates. The numerical integration of this equation is described in Section 2.2.4.

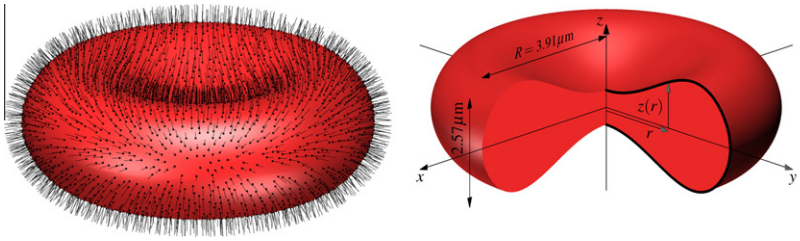

Fig. 1. The shape of a red blood cell with $R = 10$ l.u. and 3509 surface points and normal vectors (left) and dimensions and profile of a red blood cell at rest (right).

The orientation of each particle is expressed using a unit quaternion $q = (q_0, \vec{q})$ with scalar component q_0 and vector component $\vec{q} = (q_1, q_2, q_3)$. Rotation of the vector $\vec{x}$ to $\vec{x}'$ by an angle θ about the axis $\hat{v}$ (a unit vector) can be achieved by the quaternion multiplication (Schwab, 2002)

$$\vec{x}' = q \circ (0, \vec{x}) \circ \bar{q} \tag{8}$$

where

$$q = \left(\cos\frac{1}{2}\theta, \hat{v}\sin\frac{1}{2}\theta\right) \tag{9}$$

and $\bar{q} = (q_0, -\vec{q})$. By expanding Eq. (8), the rotation can be expressed in matrix form as $\vec{x}' = \mathbf{S}\vec{x}$, where $\mathbf{S}$ is (Schwab, 2002):

$$\mathbf{S} = \begin{bmatrix} 1-2(q_2^2+q_3^2) & 2(q_1q_2 - q_0q_3) & 2(q_1q_3 + q_0q_2) \\ 2(q_2q_1 + q_0q_3) & 1-(q_1^2+q_3^2) & 2(q_2q_3 - q_0q_1) \\ 2(q_3q_1 - q_0q_2) & 2(q_3q_2 + q_0q_1) & 1-2(q_1^2+q_2^2) \end{bmatrix} \tag{10}$$

If $\vec{x}$ is the position of a point in body-fixed coordinates on an object with orientation given by q, then $\vec{x}'$ is the position of that point in the lattice reference frame, provided that both coordinate systems share the same origin (otherwise a translation is required). By differentiation of Eq. (8) with respect to time, the rate of change of orientation due to an angular velocity $\vec{\omega} = (\omega_1, \omega_2, \omega_3)$ in body fixed coordinates is (Schwab, 2002):

$$\dot{q} = \frac{1}{2} q \circ (0, \vec{\omega}) \tag{11}$$

This can be written as:

$$\dot{q} = \frac{1}{2}\begin{bmatrix} 0 & -\omega_1 & -\omega_2 & -\omega_3 \\ \omega_1 & 0 & \omega_3 & -\omega_2 \\ \omega_2 & -\omega_3 & 0 & \omega_1 \\ \omega_3 & \omega_2 & -\omega_1 & 0 \end{bmatrix}\begin{bmatrix} q_0 \\ q_1 \\ q_2 \\ q_3 \end{bmatrix} \tag{12}$$

The eigenvalues of the matrix in Eq. (12) are purely imaginary, making explicit Euler integration of Eq. (12) unstable. However, explicit Euler integration can be used if q is scaled in each time step to ensure that it remains a unit quaternion. For higher accuracy, modified Euler integration, a second order Runge–Kutta method, can be used (Suzuki and Inamuro, 2011). Fourth order Runge–Kutta integration is conditionally stable for imaginary eigenvalues and could be used, but it requires more computational operations. An explicit solution for the quaternion rate of change equation (Eq. (11)) is available for constant angular velocity (Phillips, 2001), eliminating the need for a numerical method:

$$q_{k+1} = q_k \circ \exp\left(\frac{1}{2}\vec{\omega}, \Delta t\right) \tag{13}$$

Applying the Euler identity for quaternions

$$\exp(\vec{x}\theta) = \cos\theta + \vec{x}\sin\theta, = (\cos\theta, \vec{x}\sin\theta,) \tag{14}$$

where $\vec{x}$ is any vector, we obtain:

$$q_{k+1} = q_k \circ \left(\cos\left(\frac{1}{2}, \Delta t\right), \vec{\omega}\sin\left(\frac{1}{2}\Delta t\right)\right) \tag{15}$$

At the time the simulation code was developed, the authors were not aware of the exact solution, and modified Euler integration with renormalization was used to solve Eq. (11) (as in Suzuki and Inamuro (2011)). Evaluating the advantages of the exact solution is left for future work.

2.2.3. Collision handling

The same surface points required for the immersed boundary method can be used to apply repulsive forces that prevent overlap between approaching particles, thereby providing a mechanism for collision handling. This section describes the choices made regarding the parameters of this collision handling method and the impacts of these parameters on the behavior of colliding particles.

Repulsive forces are applied between all pairs of surface points that are located within a threshold distance of each other and belong to different particles. A linked list is used to speed up the search for nearby surface points. The repulsive force acts at the position of the surface point in the direction of the inward normal. Thus, the direction of the normal at each surface point must be stored and updated at each time step together with the surface points. The repulsive force was chosen to vary linearly with the separation distance. Thus the collisional force acting at a surface point is:

$$\vec{F}_{s,i} = \sum_{\substack{j \\ \|\vec{x}_i - \vec{x}_j\| < \delta}} k\left(\delta - \|\vec{x}_i - \vec{x}_j\|\right)(-\hat{n}_i) \tag{16}$$

where k specifies the strength of the repulsive force, δ is the threshold distance, $\hat{n}_i$ is the outward normal of the surface at the position $\vec{x}_i$ of the i^{th} surface point. Only those j corresponding to surface points on particles other than the one with the i^{th} point are considered. Due to the random distribution and finite number of surface points, the method effectively simulates rough surfaces. Consequently, post-collision trajectories of spheres, for example, will depend on their relative orientations despite their symmetry because of the positioning of surface points along the surface. This is a desirable feature when the real surfaces are not perfectly smooth.

The behavior of colliding particles and the effectiveness of the method depend on several parameters. These are the threshold distance δ, the distribution of surface points, and the magnitude of the proportionality factor k. The distance threshold δ was fixed at half the lattice spacing, considering the inherently finite resolution of the LBM flow solver. The number of surface points must be sufficient to resolve the shape of the particle. Since this condition must also be met by the surface points for the immersed boundary method, the same points can be used for the immersed boundary method and for collision handling. A higher surface point density is expected to reduce the roughness of the surfaces. Several test simulations with multiple colliding spheres arranged horizontally showed insignificant vertical deviation until approximately five collisions. The number of surface points had to be increased by a factor of eight to raise this number of collisions to about ten. This large number of surface points increased the execution time significantly. The same number of surface points was therefore used for

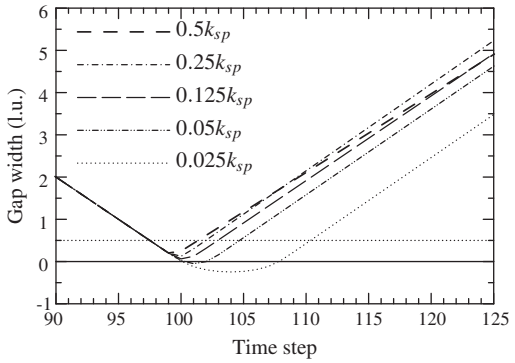

Fig. 2. Gap width as a function of time during the collision between two particles under several repulsive force strengths expressed as fractions of k_{sp} (Eq. (17)). The dotted horizontal line shows the threshold distance $\delta = 0.5$.

the immersed boundary method and for collision handling. As illustrated in Fig. 1, 3509 points were used on the RBC surface, corresponding to a typical spacing of 0.5 l.u. ($0.05R$) between surface points. This number of surface points provided sufficiently smooth collisions and a reasonable execution time on modern hardware.

To determine the required strength of the repulsive force field, we can consider the simplified case of two spheres of mass m, each approaching the midpoint between them at a speed u. We suppose that each sphere has only one surface point located at the point nearest the other sphere. To determine the force field strength required to stop the particles over a distance δ, we can consider an energy balance between the initial kinetic energy of the spheres and the potential energy stored when the particles have stopped. As a result, the minimum field strength for a single pair of surface points k_{sp} is:

$$k_{sp} = 2\frac{mu^2}{\delta^2} \tag{17}$$

When the particles are immersed in fluid, the required force increases due to the mass of fluid that moves with the particles and decreases due to lubrication forces in the gap between the particles. Though Eq. (17) does not account for these effects, we use Eq. (17) as a guide for selecting k in simulations with fluid. In dry simulations we consider the fact that several pairs of surface points become active as two particles collide. As a result, the minimum spring strength that is required to stop particles with many surface points is lower than k_{sp}. Fig. 2 shows the separation distance as a function of time between two particles shaped as RBCs involved in a head-on collision (without fluid). Several fractions of k_{sp} were considered. The initial speed of the particles was 0.1 length units per time step. It can be seen that the minimum field strength (k in Eq. (16)) required to prevent overlap is slightly higher than 5% of k_{sp}. It is also evident that reducing the strength of the forcing results in "softer" collisions. The choice of maximum velocity u in LB simulations is based on the maximum expected flow velocity, which must be limited to ensure that incompressible flow is simulated. A field strength k equal to 0.15 k_{sp} for a maximum velocity of 0.1 (u in Eq. (17)) was used in the dense suspension simulations. The factor of 0.15 was chosen because it is higher than the minimum required to prevent overlap (0.05), and energy conservation is good, as is discussed in Section 2.2.5. Lubrication forces or other attractive and repulsive surface forces were not implemented in the present simulations but could be added to the current framework.

Sedimentation simulations of spheres involve a calibration step to account for the discretization of the interface with a finite number of surface points and the interpolation of the immersed boundary force from the surface points to the lattice nodes. The need for a viscosity-dependent calibration was shown by Ladd (1994), and a method for performing such a calibration is described in ten Cate et al. (2002) and Derksen and Sundaresan (2007). Such a calibration to determine the effective size of the non-spherical particles was not used for the analyses that follow due to the lack of an accurate drag force model with which the simulations could be calibrated. For spheres, the drag force on a periodic array of spheres is used (Sangani and Acrivos, 1982). We therefore estimate (based on e.g. ten Cate et al. (2002)) an upper bound for the error in the particle radii of ±0.5l.u. When $R = 10$, this corresponds to a 5% error in the radius, a 10% error in the surface area, and a 15% error in the volume of each particle and therefore the solids volume fraction. We keep this error estimate in mind when analyzing the sedimentation results.

2.2.4. Stability at low density ratios

As the solid density approaches the fluid density, the integration of Eqs. (4) and (7) becomes difficult because the difference on the left side approaches zero. To analyze the stability and accuracy of integration methods for these equations, we consider the model problem:

$$(\gamma - 1)\frac{dy}{dt} = -\lambda y \tag{18}$$

To apply the subsequent stability and accuracy analysis to Eq. (5), we can linearize Eq. (5) and find that y is related to a component of the velocity and γ is the density ratio. The (positive real) parameter λ is given by

$$-\lambda = \frac{1}{\rho_f V}\frac{\partial F}{\partial y} \tag{19}$$

where F is the integral over V of the component of $\vec{f}$ that is in the same direction as the velocity component chosen for y. The quantity $\frac{\partial F}{\partial y}$ is negative because F is a drag force: its magnitude increases as the velocity increases and it acts in the direction that is opposite to the particle velocity. The analysis is restricted to $\gamma > 1$; otherwise the solution to Eq. (18) grows exponentially. We do not consider the forcing term $(\gamma - 1)\vec{g}$ since the stability of a differential equation is generally determined by the eigenvalues and not the source terms. With explicit Euler integration, Eq. (5) becomes:

$$\vec{v}_{k+1} = \vec{v}_k + \left(\frac{1}{(\gamma - 1)\rho_f V}\int_V \vec{f}\,dV + \vec{g}\right)\Delta t \tag{20}$$

The explicit Euler discretization of the model problem is:

$$y_{k+1} = \left(1 - \frac{\lambda \Delta t}{\gamma - 1}\right) y_k \tag{21}$$

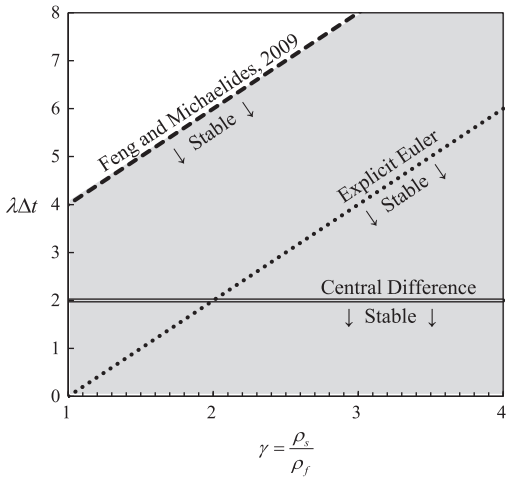

Fig. 3. Stability regions of the three integration methods.

The condition for stability is:

$$\lambda\Delta t < 2(\gamma - 1) \tag{22}$$

Feng and Michaelides (2009) proposed a method for achieving stability at low density ratios that involves evaluating one of the derivatives in Eq. (5) at the previous time step:

$$\vec{v}_{k+1} = \left(1 + \frac{1}{\gamma}\right)\vec{v}_k - \frac{1}{\gamma}\vec{v}_{k-1} + \left(\frac{1}{\rho_s V}\int_V \vec{f}\,dV + \left(1 - \frac{1}{\gamma}\right)\vec{g}\right)\Delta t \tag{23}$$

We call such methods that involve the evaluation of the two derivatives in different ways split-derivative methods. Applying this approach to the model system, Eq. (18), yields

$$y_{k+1} = \left(1 + \frac{1}{\gamma}\right)y_k - \frac{1}{\gamma}y_{k-1} - \frac{\lambda}{\gamma}y_k\Delta t \tag{24}$$

The condition for stability is:

$$\lambda\Delta t < 2(\gamma + 1) \tag{25}$$

Instead of using two one-sided finite differences, one of the differences can be a central difference. With such a discretization, stability at low density ratios is also achieved. Using a central difference for the first derivative term on the left of Eq. (5) and a backward difference for the second provides:

$$\vec{v}_{k+1} = \left(1 - \frac{2}{\gamma}\right)\vec{v}_{k-1} + \frac{2}{\gamma}\vec{v}_k + 2\left(\frac{1}{\rho_s V}\int_V \vec{f}dV + \left(1 - \frac{1}{\gamma}\right)\vec{g}\right)\Delta t \tag{26}$$

With this method, the discrete form of the model problem is

$$y_{k+1} = \left(1 - \frac{2}{\gamma}\right)y_{k-1} + \frac{2}{\gamma}y_k - \frac{2}{\gamma}\lambda y_k\Delta t \tag{27}$$

and the stability criterion is

$$\lambda\Delta t < 2 \tag{28}$$

Interestingly, stability does not depend on the density ratio γ.

The stability regions for the three methods are compared in Fig. 3. The benefits of the two split-derivative methods are clear: they remain stable at low γ unlike the explicit Euler method. Though the present stability analysis cannot be used for $\gamma < 1$, the split-derivative methods are stable for $\gamma < 1$. Feng and Michaelides (2009) presented a simulation of a rising light particle, and a test simulation showed that the same is possible with the central difference split-derivative method.

The accuracy of the three methods is compared in Fig. 4 for two values of λ (0.01 and 0.3) and three values of γ (1.1, 1.6, and 2.5). The time step was $\Delta t = 1$. Explicit Euler integration is unstable for $\lambda = 0.3$ and $\gamma = 1.1$; it is therefore not shown. It can be seen that the central difference split-derivative method is generally more accurate than the method of Feng and Michaelides (2009) for the model problem, considering the lower oscillation amplitudes. For the lower value of λ, explicit Euler integration is the most accurate; the two split-derivative methods oscillate when $\gamma = 1.1$. The three methods provide very close solutions for $\gamma = 1.6$ and $\gamma = 2.5$.

A representative value for λ was obtained by simulating the settling of a single sphere (diameter $D = 14$) in a fully periodic cubic domain (64^3) with a fluid of kinematic viscosity 0.01 and density 8.0, and a gravitational acceleration of 5×10^{-5}. These values are given in lattice units, with the lattice spacing and time step both being one. The sphere had 3832 uniformly-distributed surface points. The initial velocity was zero, and the velocity at the previous time step was also initialized to zero. Only the vertical (parallel to gravity) velocity was integrated; the other two translational velocities and the three angular velocities were fixed at zero. The simulations were run using the Feng and Michaelides (2009) method and the central difference method at density ratios of 1.1, 1.6, and 2.5. Explicit Euler integration was only stable for $\gamma = 2.5$. The seven simulations provided a value of about 0.3 for λ, obtained by using Eq. (19) and estimating the slope from a plot of the force as a function of velocity. Though the velocity evolution showed slightly less oscillation with the central difference method, the force showed more oscillation. The increased oscillation in the force applied on the particle may be due to the immersed boundary method in which the force is proportional to changes in velocity. It would therefore be interesting to test the method with a different immersed boundary condition implementation such as direct forcing (Wang et al., 2008). Overall, for the model problem, we see that as λ decreases and γ increases, the methods converge to the exact

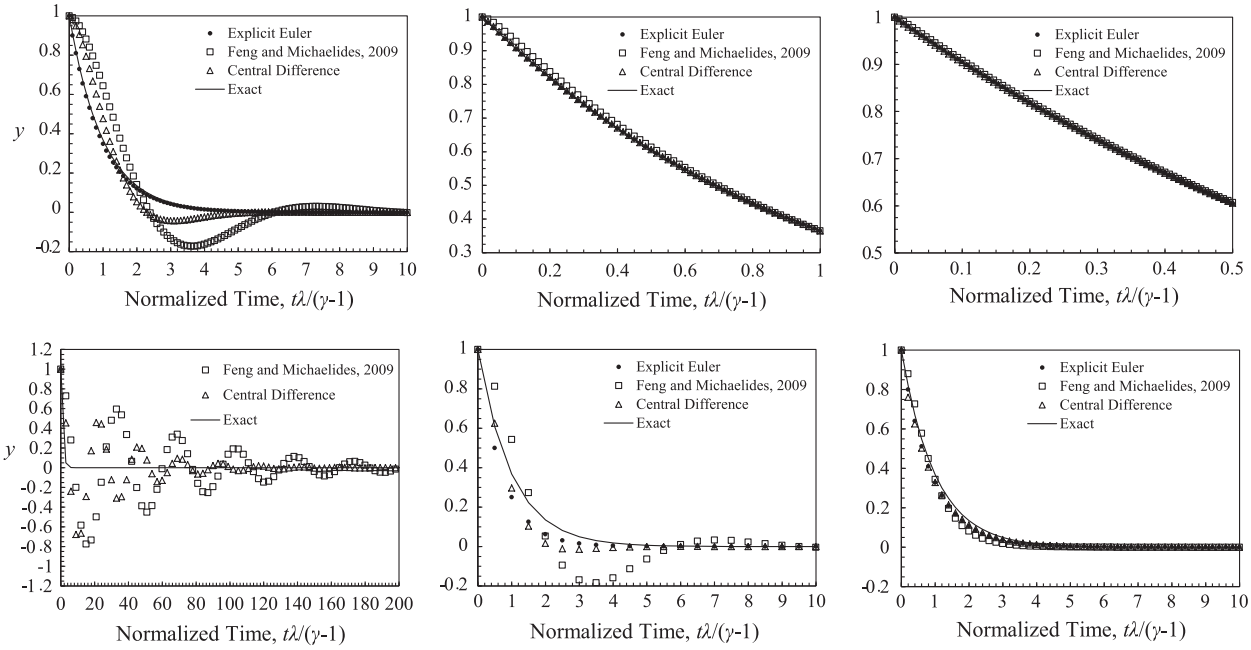

Fig. 4. Numerical and exact solutions of the model problem for $\gamma = 1.1$ (left), 1.6 (centre), and 2.5 (right) and $\lambda = 0.01$ (top) and 0.3 (bottom).

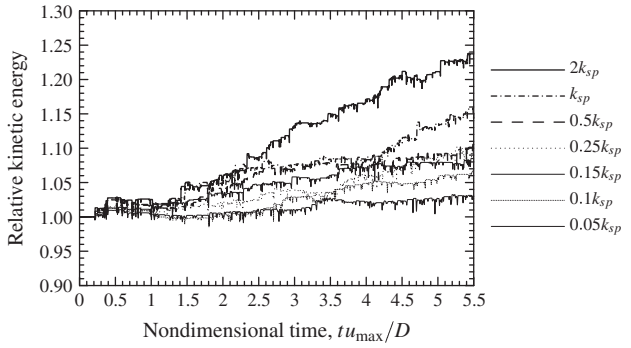

Fig. 5. Kinetic energy relative to the initial kinetic energy as a function of time for several repulsive force strengths expressed as fractions of k_{sp}.

solution. With $\lambda = 0.3$ and $\gamma = 1.1$, significant oscillation is evident with the split-derivative methods, but explicit Euler integration is unstable. Comparing explicit Euler integration with the split-derivative methods, the gain in stability achieved by using a split-derivative method is offset by a loss of accuracy. Comparing the two split-derivative methods, the central difference method has higher accuracy but a smaller stability region. The numerical results are consistent with the previously given stability criteria.

The simulations of a single settling sphere showed that the estimated value of λ rapidly decreases by several orders of magnitude after about 10 time steps. Therefore, it may be possible to use the more stable but less accurate methods only at the beginning and use a higher accuracy method once λ decreases sufficiently. However, with multiple particles in a dense suspension, sudden changes in velocity due to collisions can temporarily increase λ, meaning that a stable method must be used always. If explicit Euler integration were used, the velocity integration would become unstable initially or after a collision. Thus, the gain in stability achieved by using a split-derivative method is very useful particularly in simulations of dense suspensions; the loss of accuracy due to using such a method only occurs during the few time steps when λ is high. The single particle sedimentation simulations showed nearly identical results for the velocity as a function of time with both split-derivative methods: after three time steps, the relative difference is less than 10%, drops below 0.1% after 200 time steps, and decreases to 0.01% after 800 time steps. For the case that was stable with explicit Euler integration ($\gamma = 2.5$), the two split-derivative methods were within 10% of the explicit Euler solution after three time steps. While the relative error of the Feng and Michaelides (2009) method compared with explicit Euler integration fell to 0.1% after about 200 time steps, the central difference method reached 0.1% after about 100 time steps. This is consistent with Fig. 4, which shows that the central difference method is slightly more accurate.

Due to the improved accuracy of the central difference split-derivative method, this method was used for the simulations of particles with low density ratios. The discretization of the linear velocity is given by Eq. (26); the discretized form of the angular velocity equation (Eq. (7)) is:

$$\vec{\omega}_{k+1} = \vec{\omega}_{k-1} + \frac{2}{\gamma}(\vec{\omega}_k - \vec{\omega}_{k-1}) + 2\Delta t I^{-1}\mathbf{S}^{-1}\int_V (\vec{x} - \vec{x}_c) \times \vec{f}\, dV - 2\Delta t\left(1 - \frac{1}{\gamma}\right) I^{-1}\vec{\omega}_k \times (I\vec{\omega}_k) \tag{29}$$

To summarize the numerical methods for low density ratio simulations, the position of the particles is updated with an explicit Euler step using the velocity, the orientation is updated using modified Euler integration of Eq. (12), the translational velocity is updated according to Eq. (26), and the angular velocity is updated according to Eq. (29). The total forces and torques acting on each particle are determined using the collisional and hydrodynamic forces at each surface point.

2.2.5. Energy conservation

Several simulations were used to assess energy conservation with the previously described collision handling method. Fig. 5 shows the total kinetic energy of the particles relative to the initial kinetic energy. The kinetic energy was computed as the sum over all particles of the translational and rotational kinetic energies:

$$E_{tot} = \frac{1}{2}\sum_i \left[m\|\vec{v}_i\|^2 + \vec{\omega}_i^T I \vec{\omega}_i\right] \tag{30}$$

The simulations involved 300 randomly-placed RBC-shaped particles with a diameter D of 20 and a density of 4.0 in a periodic 132^3 domain for 5000 time steps. The solids volume fraction was 20.5%. The strength of the force field was based on a velocity of 0.05 and a threshold distance of 0.5. The particles were given random initial translational and rotational velocities. Each component of the translational velocity was chosen from $[-0.0125, 0.0125]$, corresponding to a maximum translational speed u_{max} of 0.022. The components of the angular velocity were chosen from $[-0.00125, 0.00125]$, for a maximum angular speed of 0.0022. The maximum initial velocity of a point on the surface of a particle was therefore 0.044. Explicit Euler integration was used for the positions and velocities of the particles. Modified Euler integration with renormalization was used for the quaternions.

It can be seen that the kinetic energy of the particles increases gradually with time, particularly with stronger repulsive forces. We attribute this to the increase in integration error for the explicit Euler method with increasing spring stiffness. For simulations with a force strength equal to or less than the minimum required strength, k_{sp}, the kinetic energy increases by 10% over 5000 time steps, which corresponds to $5.5D/u_{max}$. For a force strength of $0.05k_{sp}$, the energy increase is only about 2%. Increasing the stiffness of the spring-like repulsive force in general increases the rate of kinetic energy generation. In these "dry" simulations, there was no interstitial fluid. In simulations with fluid, it is expected that the fluid would dissipate the energy that is generated. Furthermore, hydrodynamic forces would reduce the relative velocities of approaching particles. One final feature of Fig. 5 is noteworthy: the regular spikes in the kinetic energy are due to collisions which temporarily convert kinetic energy to potential energy in the repulsive force field between surface points.

Considering the energy conservation results and collision trajectories, the simulations of dense particulate suspensions were performed using a maximum speed of 0.1 and a force strength of $0.15k_{sp}$. At this force strength, the collisions are reasonably rigid (Fig. 2), and energy conservation is good (less than a 10% increase after 5000 time steps in the dry simulation).

3. Simulation results and discussion

The previously described methods were first used to simulate single rigid RBC-shaped particles and then dense suspensions of rigid RBCs. Though we use RBCs as an example of a non-spherical particle and do not run simulations with parameters that match sedimenting blood exactly, the properties of blood are given here as they are useful for evaluating the differences between the simulations and erythrocyte sedimentation tests. Furthermore, the choices of solids volume fraction and density ratio were inspired by the properties of blood.

Blood is primarily a suspension of red blood cells in a Newtonian fluid called the plasma. Other cells, such as white blood cells, are present in smaller quantities: there is approximately one white

blood cell per 600 red blood cells (Elad and Einav, 2003). A typical volume fraction of red blood cells, the hematocrit, is 45%. The dynamic viscosity of the plasma ranges between 0.0011 and 0.0016 Pa.s; the density is 1.03 g/cm^3 (Elad and Einav, 2003). The midpoint of the viscosity range was used to obtain an estimated kinematic viscosity of 1.31×10^{-6} m^2/s. Red blood cells are only slightly denser than the plasma, having a density of 1.10 g/cm^3, resulting in a density ratio of 1.07 (Elad and Einav, 2003). The profile shape of red blood cells at rest can be described using (Evans and Fung, 1972):

$$z(r) = \frac{1}{2}\sqrt{1-\left(\frac{r}{R}\right)^2}\left(C_0 + C_2\left(\frac{r}{R}\right)^2 + C_4\left(\frac{r}{R}\right)^4\right) \tag{31}$$

where R is 3.91 μm, C_0 is 0.81 μm, C_2 is 7.83 μm, and C_4 is −4.39 μm. The (major) diameter $D = 2R$ is 7.82 μm and was chosen to span 20 lattice spacings, thereby fixing the lattice length scale at one lattice spacing per 0.391 μm. The moments of inertia about the principal axes were obtained by symbolic integration. The shape was illustrated in Fig. 1. With $R = 10$ l.u., the surface area is 877 l.u.^{2}, and the volume is 1574 l.u.^{3}. A commonly-used property of non-spherical particles that is relevant to studies of sedimentation is the sphericity S, given by

$$S = \frac{A_s}{A_p} \tag{32}$$

where A_s is the surface area of a sphere with the same volume as the particle, and A_p is the surface area of the particle. For the RBC shape, the sphericity is 0.75.

3.1. Sedimentation of one particle

The use of the LBM and immersed boundary method described in this paper has been evaluated elsewhere for spherical particles (ten Cate et al., 2002; Derksen and Sundaresan, 2007). After calibrating the particle diameter, excellent quantitative agreement was obtained. Therefore only simulations with non-spherical particles will be discussed in this paper. Simulations of one settling RBC-shaped particle were used to assess the immersed boundary and motion integration methods for non-spherical particles. Two different Reynolds numbers were considered. In both simulations, the particle diameter D was 20, the fully periodic domain was $320 \times 64 \times 64$ ($16D \times 3.2D \times 3.2D$; first dimension parallel to gravity), and the density ratio γ was 1.05. In these and all further sedimentation simulations, a body force was applied to the fluid to ensure that the forces on the simulated domain are balanced (Derksen and Sundaresan, 2007). The terminal Reynolds number was manipulated by changing the viscosity of the fluid and the gravitational acceleration while ensuring that the terminal speed remained approximately the same and did not exceed 0.01 in lattice units. Limiting the speed ensures that incompressible flow is simulated.

A terminal Reynolds number ($\mathrm{Re}_\infty = u_\infty D/\nu$) of 7.3 was obtained for the terminal velocity (u_∞) of 0.0037 with a viscosity of 0.01 and a gravitational acceleration of 1.8×10^{-4} (dimensional quantities without specified units are in lattice units). With a viscosity of 0.1 and an acceleration of 1.8×10^{-3}, the terminal speed was 0.0058, corresponding to a Reynolds number of 1.2. The terminal velocities are relative to a stationary observer rather than the fluid. With only one particle, the required upward force to maintain an overall force balance is small and produces a low (more than an order of magnitude lower than the particle velocity) net upward flow rate that was therefore neglected. The speed of the upward flow is included in the analysis of the dense suspension sedimentation simulations described below. Fig. 6 shows a sequence of cross sections of the flow field. The first image in each sequence shows the initial condition; the final image shows the steady-state condition. Fig. 7 shows the particle Reynolds number Re as a function of time. Both simulations ran for 100,000 time steps ($18.5D/u_\infty$ for the higher Reynolds number and $29D/u_\infty$ for the lower Reynolds number). Fig. 8 shows the angular velocity about the axis out of the page (Fig. 6).

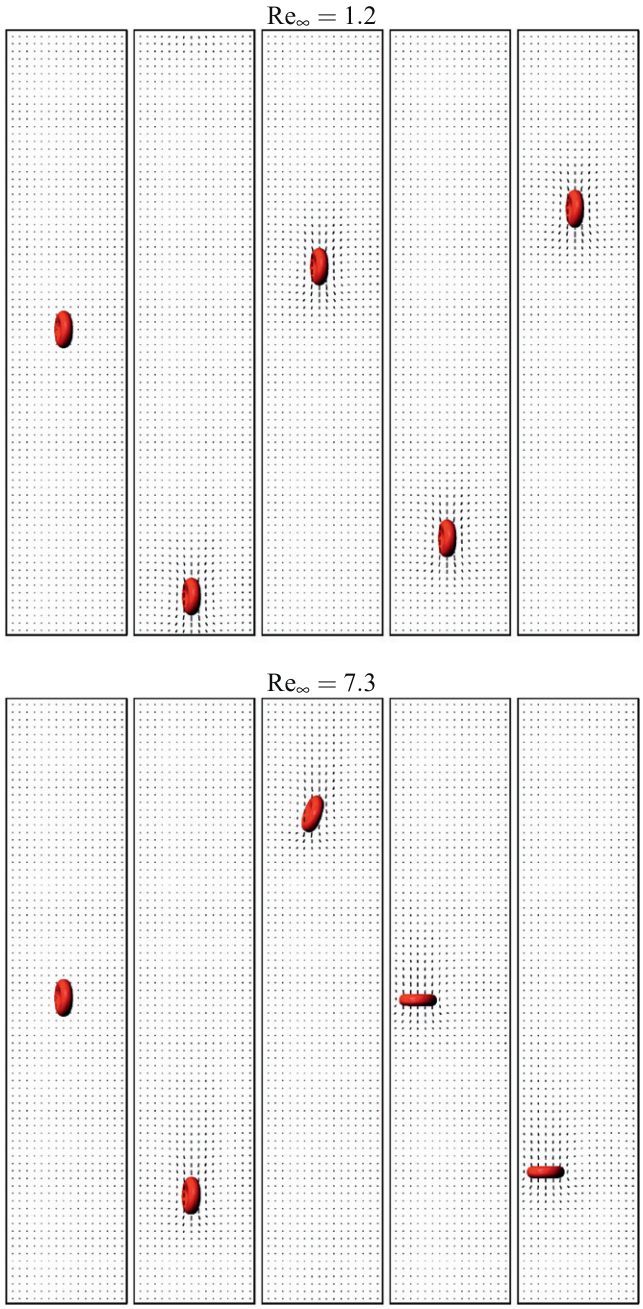

Fig. 6. Sedimentation of a single particle at a Reynolds number of 1.2 (upper sequence) and 7.3 (bottom sequence) with time progressing from left to right.

At the lower Reynolds number of 1.2, the particle settles in a vertical orientation which minimizes the projected surface area perpendicular to the flow direction. At the higher Reynolds number (7.3), the particle flips to a horizontal orientation with maximal projected area. This is consistent with the ranges given by Becker (1959). The RBC-shaped particle should be stable in any orientation for $\mathrm{Re}_\infty < 6.6$. For $6.6 < \mathrm{Re}_\infty < 240$, the particles are expected to settle in the horizontal orientation. At higher Reynolds numbers, the particles would exhibit wobbling and rotation. Thus, the simu-

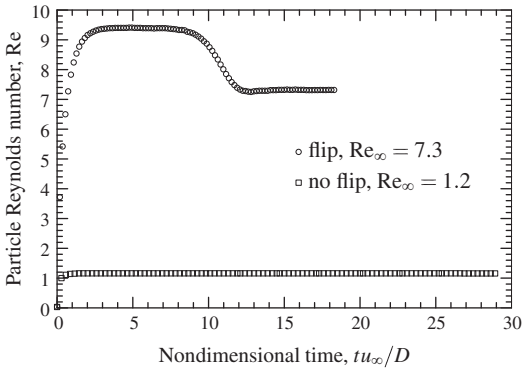

Fig. 7. Particle Reynolds number as a function of time.

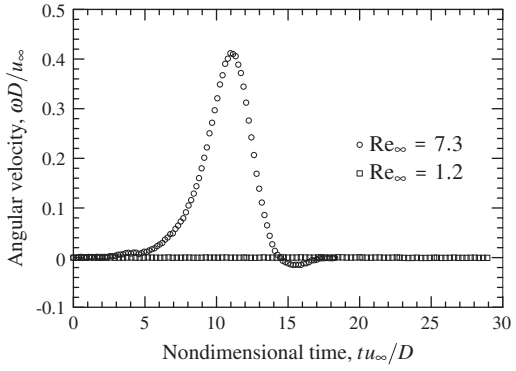

Fig. 8. Angular velocity as a function of time about the axis out of the page in Fig. 6.

lation results agree with the expected behavior: the transition from vertical to horizontal settling occurs over the expected Reynolds number range. The existence of a transition regime between 1.2 and 7.3 is also consistent with work on disk sedimentation in non-Newtonian fluids by Walker and Mayes (1975) and by Peden and Luo (1987).

We can also compare the drag coefficients obtained from the simulations with literature values. We use the drag coefficient C_D defined as

$$C_D = \frac{2F_D}{\rho_f u_\infty^2 A_\perp} \tag{33}$$

where F_D is the drag force and $A_\perp$ is the projected area perpendicular to the flow direction. At steady state, the drag force is balanced by the net weight (weight minus buoyancy), which leads to:

$$C_D = \frac{2}{\pi}\frac{gV_p}{u_\infty^2 R^2}(\gamma - 1) \tag{34}$$

where V_p is the volume of the particle. For the horizontal settling orientation (Re = 7.3) the drag coefficient from the simulation is 6.6. Considering the high sphericity and the similarity between the drag coefficients for spheres and disks settling horizontally at Re < 10 (Lapple and Shepherd, 1940), we compare the drag coefficient at Re = 7.3 with the value for a sphere, 5.1. We judge this agreement to be reasonable considering the difference in shape, the 5% error estimate for the radius, and the finite size and periodicity of the domain. Due to the periodicity and high aspect ratio (height over width) of the domain, we are effectively simulating an infinite horizontal array of disks rather than a single particle in an infinite domain. The effect of this periodicity is the reason for using the drag on a cubic array of spheres for the calibration of LBM simulations of spherical particles. We cannot calibrate arbitrarily shaped particles in the same way due to the absence of accurate drag force values for periodic arrays.

3.2. Simulations of dense suspensions

As in simulations of dense suspensions of spheres, a compaction procedure is required to obtain a random initial distribution of particles with a high solids fraction. At the start of the compaction procedure, particles are distributed randomly in a region that is much larger than the desired final simulation domain. The particles are given random initial translational and rotational velocities, and a force field pulls the particles to the centre. The potential energy of the particles due to the force field must be dissipated so that the particles eventually stop. This was achieved by reducing the velocities of the particles by a small fraction in each time step. The compaction process used to achieve a solids volume fraction of 45% is illustrated in Fig. 9. Since the solids fraction was higher than 45% at the end of the initial compaction simulation, the particle positions and orientations were used in a second simulation. In this simulation, the particles were given random initial velocities, they were allowed to fill a larger domain, and were then "cooled" until they were stationary.

3.2.1. Effect of solids volume fraction

We now consider the fully coupled simulations of dense suspensions and evaluate the effect of the solids volume fraction on the sedimentation rate and particle orientation. A fluid domain of $320 \times 64 \times 64$ lattice units (or $16D \times 3.2D \times 3.2D$, with the first dimension parallel to gravity) was used. The system can be characterized with four dimensionless parameters. These are: the solids volume fraction ϕ, the density ratio γ, the Reynolds number $\mathrm{Re} = u_\infty D/\nu$, and the Froude number $\mathrm{Fr} = u_\infty^2/gD$. Four values of ϕ were used: 0.30, 0.35, 0.40, and 0.45. The particle positions and orientations for the three simulations with $\phi < 45\%$ were obtained by omitting randomly selected particles from the results of the compaction procedure that provided $\phi = 0.45$. The density ratio

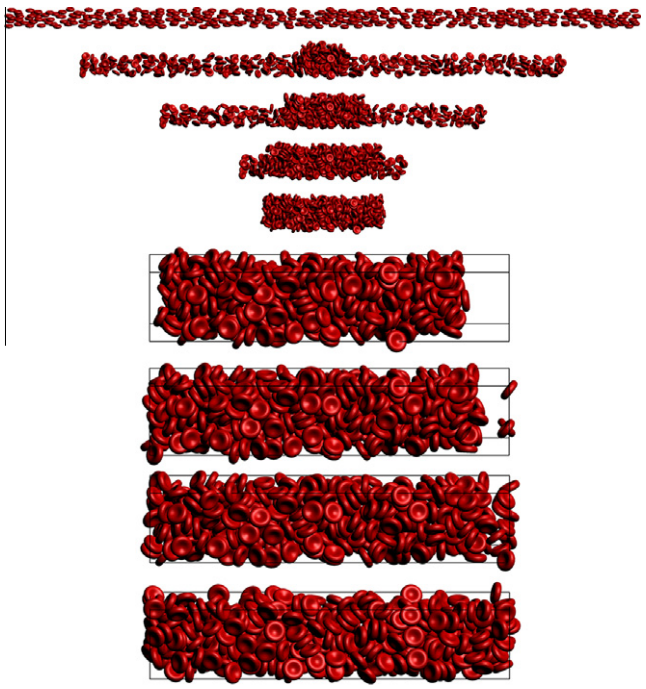

Fig. 9. Compaction (top) and expansion (bottom, enlarged) simulations used to achieve a solids volume fraction of 45%.

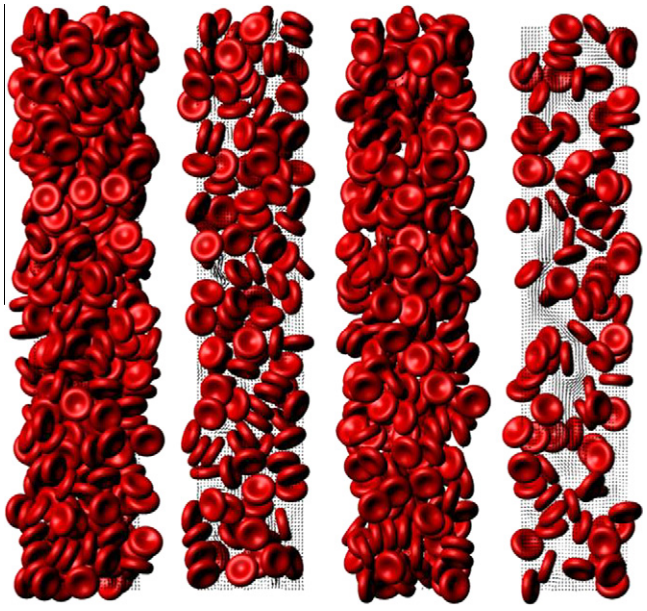

Fig. 10. Particle positions and flow field cross-sections after 100,000 time steps for the simulations with $\phi = 0.45$ (left pair) and 0.35 (right pair). The flow field is emphasized in the right image of each pair by hiding all particles farther than one particle radius from the cross-section plane.

was fixed at $\gamma = 1.07$. The average particle Reynolds number at steady state is an output of the simulations. To consider the effect of gravity without including the settling speed, we use the dimensionless quantity $\mathrm{Re}^2/\mathrm{Fr} = gD^3/\nu^2$ instead of the Froude number. This number depends entirely on input parameters for the simulations. For all four simulations, the kinematic viscosity was 0.01 and the gravitational acceleration was 1.8×10^{-4}, resulting in $gD^3/\nu^2 = 14,400$. This value would be achieved, for example, by 1.1 mm diameter particles settling in water with the gravitational acceleration on Earth. Sample visualizations of the dense suspension simulations are shown in Fig. 10.

Fig. 11 shows the average settling rate of the particles as a function of time for the four simulations. The two lower ϕ simulations ran for 300,000 time steps; the higher ϕ simulations ran for 600,000 time steps. The Reynolds number used to describe the settling rate is based on the average velocity of the particles relative to the fluid. The average relative velocity of the particles was obtained by first estimating the average upward velocity of the interstitial fluid. The total momentum of the fluid (interstitial and internal to the particles) was obtained by integrating the velocity

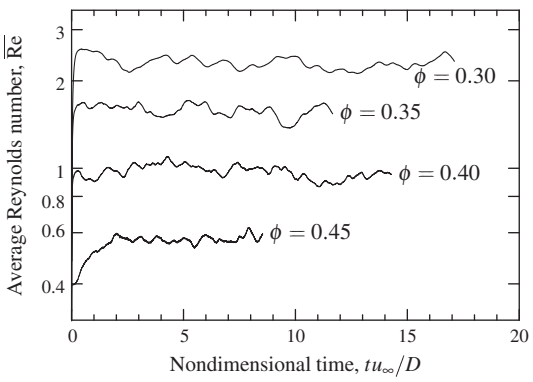

Fig. 11. Average particle Reynolds number as a function of time for four simulations at different solids volume fractions.

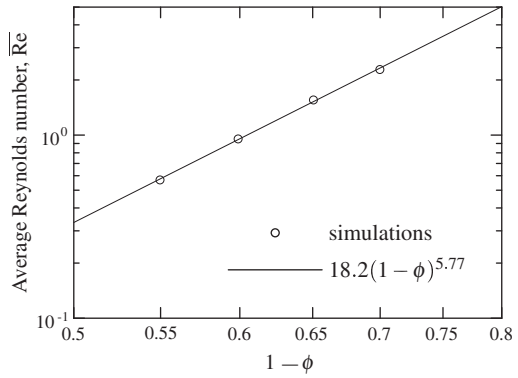

Fig. 12. Sedimentation rate (average particle Reynolds number) as a function of the void fraction $1 - \phi$. Both axes are scaled logarithmically.

over the entire fluid domain. The average velocity inside each particle is the velocity of the particle's centre of mass. By subtracting the momentum of the internal particle fluid from the total fluid momentum, we obtain the momentum of the interstitial fluid. Dividing by the total mass of the interstitial fluid then provides the average velocity of the interstitial fluid. The average sedimentation rate relative to the fluid is then the sum of the average downward speed of the particles and the average upward speed of the interstitial fluid. It can be seen that the particles rapidly reach a steady settling rate. For the highest solids fraction ($\phi = 0.45$), the approach to steady state occurs the slowest. In all cases, we see slight fluctuation about an average settling rate that depends strongly on the solids volume fraction.

The effect of the solids volume fraction on the sedimentation rate is shown in Fig. 12. The points that are shown were obtained by averaging the Reynolds numbers in Fig. 11 over the second half of the simulation time. A Richardson–Zaki (Richardson and Zaki, 1954) model was fit to the data, since this model is commonly used to analyze suspensions of monodisperse spheres. This model has the form:

$$\overline{\mathrm{Re}} = \mathrm{Re}_0(1-\phi)^n \tag{35}$$

where $\overline{\mathrm{Re}}$ is the Reynolds number for the sedimentation rate of a suspension with a solids volume fraction of ϕ, Re_0 is the terminal Reynolds number of a single particle, and n is a fitted exponent. The value of n depends on the Reynolds number; for spherical particles and $\overline{\mathrm{Re}}$ near 1 it is 4.35 (Rowe, 1987; Di Felice, 1999). A linear least squares fit was used to obtain $\mathrm{Re}_0 = 18.2$ and $n = 5.77$. For a single sphere under the same conditions Re_0 is 11.8. The reason for the higher value of the extrapolated sedimentation rate at infi-

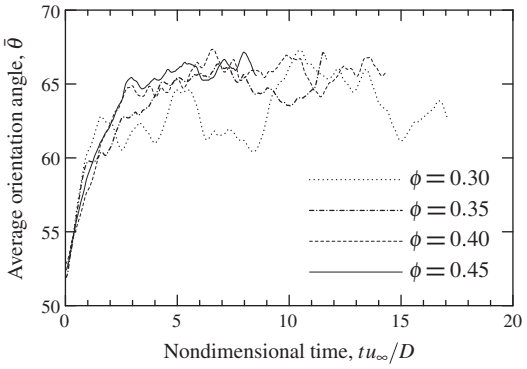

Fig. 13. Average particle orientation angle as a function of time for four simulations at different solids volume fractions.

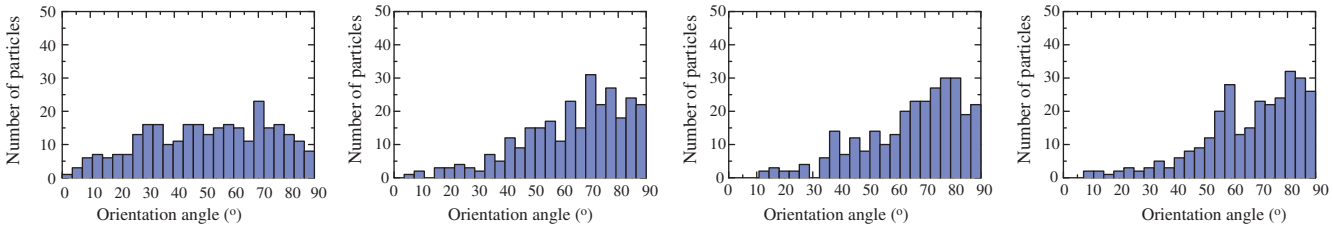

Fig. 14. Evolution of the particle orientation angle histograms for the $\phi = 0.35$ case. The initial histogram (left) and the histograms after 100,000 ($tu_\infty/D = 3.9$), 200,000 ($tu_\infty/D = 7.7$), and 300,000 time steps ($tu_\infty/D = 11.6$) are shown (left to right).

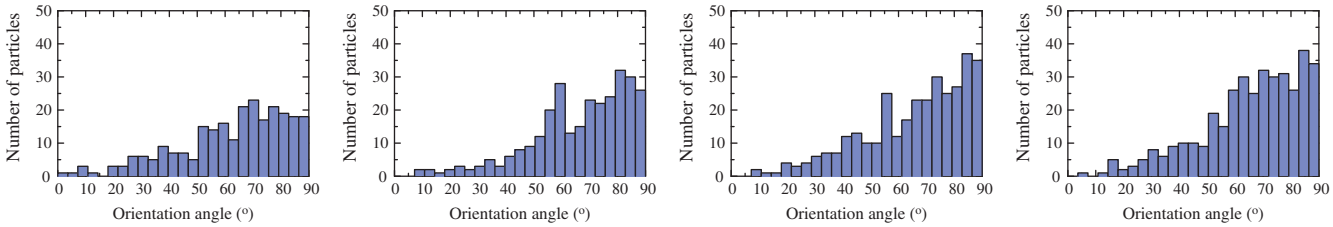

Fig. 15. Particle orientation angle histograms at the end of the simulation with (left to right) $\phi = 0.30$, $\phi = 0.35$, $\phi = 0.40$, and $\phi = 0.45$. The corresponding nondimensional times (tu_∞/D) are 17.1, 11.7, 14.3, and 8.5 respectively.

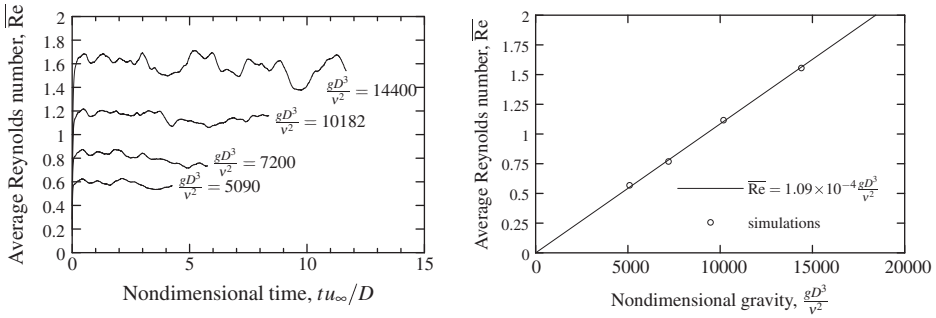

Fig. 16. Sedimentation rate as a function of time (left) for varying gravitational accelerations and the dependence of the average sedimentation rate on the gravitational acceleration (right).

nite dilution may be the vertical alignment of the particles, which is described next, that increases the settling rate. The higher exponent indicates a stronger dependence of the settling rate on the void fraction for RBC shapes when compared with spheres.

3.2.2. Particle orientation during sedimentation

While obtaining the orientation of each particle as a function of time is difficult in experiments, this data is readily available from simulations. Fig. 13 shows the average angle of the particles with respect to the settling direction. The angle θ is the angle between the $\pm z$ axis of the particle shown in Fig. 1 and the settling direction. It can be seen that the average angle changes by about 10° from the initial average. After an initial transient lasting about $5D/u_\infty$, which is significantly longer than the time to reach a steady settling rate, the average angle fluctuates significantly about an apparently steady value. As a result, we believe that the simulations have achieved a steady state in terms of the settling rate and orientation. Considering the large fluctuations in the average angle, we do not present results for the effect of ϕ or $\overline{\mathrm{Re}}$ on $\bar{\theta}$. These fluctuations have a significantly higher amplitude for the lowest solids volume fraction when the particles are free to rotate due to the increased space around them.

Figs. 14 and 15 show the probability density function of the orientation angle. In Fig. 14, the evolution from the initial, nearly-uniform, distribution to the final skewed distribution is shown for the simulation with ϕ = 0.35. Fig. 15 shows the histograms at the end of the four simulations. As the solids fraction increases, the extent of the vertical alignment increases.

4. Comparison with erythrocyte sedimentation rate

Since the shape of the particles, the solids volume fraction (hematocrit), and the density ratio of the simulations match those of blood, we briefly compare our results with the sedimentation rate of blood. The International Council for Standardization in Haematology (ICSH) recommendations for testing the erythrocyte sedimentation rate (ESR) state that the hematocrit of a blood sample should not exceed 35% (International Council for Standardization in Haematology, 1993). We therefore use the simulation with ϕ = 0.35 for comparison.

Due to computational constraints, simulations that match the value of gD^3/ν^2 for sedimenting blood while retaining the same resolution are not feasible. We therefore attempt to correct for this difference. For blood sedimenting under normal gravity, gD^3/ν^2 is 2.7×10^{-3}, a factor of 5.3×10^6 lower than in the simulations. However, we recognize that at low Reynolds numbers (creeping flow) the terminal velocity of a particle depends linearly on the gravitational acceleration. For a single sphere (e.g. Tilton (2008)),

$$18\mathrm{Re}_t = (\gamma - 1)\frac{gD^3}{\nu^2} \tag{36}$$

Provided that the Reynolds number is low (<0.1), we can therefore estimate the sedimentation rate under weaker gravity by using simulations with a higher acceleration. Since the Reynolds number in the simulation with $\phi = 0.35$ is near two and therefore exceeds 0.1, the error in the linearity assumption must be evaluated for Reynolds numbers near 2. We estimate this error to be an underestimate of 20% based on the ratio of the drag coefficient for a sphere given by Stokes' law (Eq. (36)) and the drag coefficient obtained using a correlation for higher Reynolds numbers (Tilton, 2008). Considering the Richardson–Zaki model for the relationship between the sedimentation rate of a single particle and a dense suspension, the error in the sedimentation rate of a dense suspension is also 20%. Several simulations with lower accelerations were performed to examine the effect of the gravitational acceleration on the sedimentation rate. The results are shown in Fig. 16 and confirm the expected linear relationship. The range of gravitational accelerations that was feasible to simulate is narrow, but the results indicate that the effect of non-linearity is small. The Reynolds number corresponding to a typical ESR of 4 mm/h is 6.6×10^{-6}. Dividing the Reynolds number from the simulation with $\phi = 0.35$ by 5.3×10^{6}, we obtain 2.9×10^{-7}, or a sedimentation rate of 0.18 mm/h. Based on the previous error estimate of 20%, the corrected value is 0.21 mm/h. This is about 20 times slower than the value for human blood. Since the magnitude of the correction for the moderate Reynolds number is small compared with the discrepancy, the assumption of linearity is not the main reason for the difference.

Several aspects of blood physiology are relevant to interpreting the discrepancy between the simulations and blood tests. The erythrocyte sedimentation rate varies with age. In men, it ranges between 3 mm/h at 20 years and 6 mm/h at 55 years. The range is 6–9 mm/h for women at the same ages (Wetteland et al., 1996). The ESR is known to depend on the hematocrit and plasma viscosity (Wetteland et al., 1996), as would be expected from a fluid mechanics perspective. The increase in sedimentation rate with age or disease is due to proteins in the plasma that increase the adhesion between cells (Wetteland et al., 1996). These proteins are present in blood at all ages, but attractive inter-particle forces were not included in the simulations. While normal cells experience these agglomerating forces, the simulations provide the sedimentation rate in the absence of inter-cellular forces. Given that abnormal sedimentation rates can be as much as an order of magnitude higher than normal rates (International Council for Standardization in Haematology, 1993), it seems plausible that the absence of any agglomeration-inducing forces could lower the sedimentation rate by an order of magnitude. The sedimentation rate determined in the present work could be assessed better by comparing it with the sedimentation rate of red blood cells in a medium that lacks the proteins that cause agglomeration. Furthermore, the deformation of cells (MacMeccan et al., 2009), which was not simulated, may also alter the sedimentation rate. Other reasons for the discrepancy, which are likely minor, include inaccuracies in completely matching the conditions of an ESR test, for example the temperature, variation in plasma viscosity, and the agglomerating effect of platelets. We also assume a uniform distribution of mass in the RBCs. In cells, density variations between the outer membrane and the internal fluid, modify the moment of inertia. Furthermore, we do not consider the effect of the Reynolds number on the average orientation, and therefore the sedimentation rate, when correcting for the different gravitational acceleration.

5. Conclusions

Simulations of dense suspensions (up to 45% solids volume fraction) of rigid non-spherical particles with low density ratios at moderate Reynolds numbers ($\approx$1) were performed using the lattice Boltzmann method. Two split-derivative methods, in which the rates of momentum change of the solid particle and internal fluid are evaluated using different discretizations, were evaluated for integrating the motion of particles at low particle over fluid density ratios. The proposed higher-accuracy model was used in the simulations. The immersed boundary method was used to impose a no-slip boundary condition on the surface of each particle. Collisions between particles in the dense suspensions were handled with a linear spring-like force field applied between the same Lagrangian points that were used in the immersed boundary method.

The methods were used to simulate rigid particles shaped like red blood cells. Two simulations of the sedimentation of a single vertically-oriented particle showed that the particle flips to a horizontal orientation as the terminal Reynolds number increases to 7.3 from 1.2. Simulations at solids volume fractions of 0.30, 0.35, 0.40, and 0.45 were used to study the effect of the solids volume fraction on the sedimentation rate and average orientation of the particles. A Richardson–Zaki model fit the simulation data closely. The cells adopt a preferentially vertical orientation, with the extent of the orientation increasing with increasing solids volume fraction.

Due to the similarity of the parameters in the simulations with those of blood, a simulation was compared with typical values of the erythrocyte sedimentation rate (ESR) blood test. After correcting for the difference in gravitational acceleration between the simulations and a blood test, a sedimentation rate of 0.21 mm/h was obtained. We attribute the difference between this value and a typical ESR of 3–9 mm/h to the omission of attractive inter-cellular forces from the simulations and the treatment of the RBCs as rigid particles. The study of the attractive, agglomeration-inducing forces and their effects on the sedimentation rate is left for future work.

While the simulations that were presented used particles shaped as red blood cells, the computational methods are general and could be used to investigate many other systems and phenomena, such as fluidized beds, crystallization, slurry transport, drilling mud, and erosion.

References

Arndt, M.F., 2008. A method for generating uniform point distributions on a sample surface. Nucl. Intrum. Meth. A 588, 509–513.

Becker, H.A., 1959. The effects of shape and Reynolds number on drag in the motion of a freely oriented body in an infinite fluid. Can. J. Chem. Eng. 37, 85–91.

ten Cate, A., Nieuwstad, C., Derksen, J., van den Akker, H., 2002. Particle imaging velocimetry experiments and lattice-Boltzmann simulations on a single sphere settling under gravity. J. Fluid Mech. 14, 4012–4025.

Derksen, J.J., Shardt, O., 2010. Hindered settling in thixotropic liquids. In: International Conference on Multiphase Flow. <http://conferences.dce.ufl.edu/icmf2010/>.

Derksen, J.J., Sundaresan, S., 2007. Direct numerical simulations of dense suspensions: wave instabilities in liquid-fluidized beds. J. Fluid Mech. 587, 303–336.

Di Felice, R., 1999. The sedimentation velocity of dilute suspensions of nearly monosized spheres. Int. J. Multiphase Flow 25, 559–574.

Elad, D., Einav, S., 2003. Physical and flow properties of blood. In: Kutz, M. (Ed.), Standard Handbook of Biomedical Engineering and Design. McGraw-Hill (Chapter 3).

Evans, E., Fung, Y.C., 1972. Improved measurements of erythrocyte geometry. Microvasc. Res. 4, 335–347.

Feng, Z.G., Michaelides, E., 2009. Robust treatment of no-slip boundary condition and velocity updating for the lattice-Boltzmann simulation of particulate flows. Comput. Fluids 38, 370–381.

Fonseca, F., Herrmann, H., 2004. Sedimentation of oblate ellipsoids at low and moderate Reynolds numbers. Physica A 342, 447–461.

Goldstein, D., Handler, R., Sirovich, L., 1993. Modeling a no-slip flow boundary with an external force field. J. Comput. Phys. 105, 354–366.

He, P., Mejia, A., Cheng, Z., Sun, D., Sue, H.J., Dinair, D., Marquez, M., 2010. Hindrance function for sedimentation and creaming of colloidal disks. Phys. Rev. E 81, 026310.

Herzhaft, B., Guazzelli, E., Mackaplow, M., Shaqfeh, E., 1996. Experimental investigation of the sedimentation of a dilute fiber suspension. Phys. Rev. Lett. 77, 290–293.

International Council for Standardization in Haematology, 1993. ICSH recommendation for measurement of erythrocyte sedimentation rate. J. Clin. Pathol. 46, 198–203.

Ladd, A., 1994. Numerical simulations of particulate suspensions via a discretized Boltzmann equation. Part 2: Numerical results. J. Fluid Mech. 271, 311–339.

Lapple, C., Shepherd, C., 1940. Calculation of particle trajectories. Ind. Eng. Chem. 32, 605–617.

MacMeccan, R.M., Clausen, J.R., Neitzel, G.P., Aidun, C.K., 2009. Simulating deformable particle suspensions using a coupled lattice-Boltzmann and finite-element method. J. Fluid Mech. 618, 13–39.

Peden, J., Luo, Y., 1987. Settling velocity of variously shaped particles in drilling and fracturing fluids. SPE Drilling Engineering 2, 337–343.

Phillips, W.F., 2001. Review of attitude representation used for aircraft kinematics. J. Aircraft 38, 718–737.

Richardson, J., Zaki, W., 1954. Sedimentation and fluidisation: Part I. Trans. Inst. Chem. Eng. 32, S82–S100.

Rowe, P., 1987. A convenient empirical equation for estimation of the Richardson–Zaki exponent. Chem. Eng. Sci. 42, 2795–2796.

Sangani, A., Acrivos, A., 1982. Slow flow through a periodic array of spheres. Int. J. Multiphase Flow 8, 343–360.

Schwab, A.L., 2002. Quaternions, Finite Rotation and Euler Parameters. <http://audiophile.tam.cornell.edu/als93/Publications/quaternion.pdf> (accessed 15.03.12).

Somers, J.A., 1993. Direct simulation of fluid flow with cellular automata and the lattice-Boltzmann equation. Appl. Sci. Res. 51, 127–133.

Suzuki, K., Inamuro, T., 2011. Effect of internal mass in the simulation of a moving body by the immersed boundary method. Comput. Fluids 49, 173–187.

Tilton, J.N., 2008. Fluid and particle dynamics. In: Green, D.W., Perry, R.H. (Eds.), Perry's Chemical Engineers' Handbook, eighth ed. McGraw-Hill (Chapter 6).

Walker, R., Mayes, T., 1975. Design of muds for carrying capacity. J. Petrol. Technol. 27, 893–900.

Wang, Z., Fan, J., Luo, K., 2008. Combined multi-direct forcing and immersed boundary method for simulating flows with moving particles. Int. J. Multiphase Flow 34, 283–302.

Wetteland, P., Roger, M., Solberg, H.E., Iversen, O.H., 1996. Population-based erythrocyte sedimentation rates in 3910 subjectively healthy Norwegian adults. A statistical study based on men and women from the Oslo area. J. Intern. Med. 240, 125–131.

Whalley, W., Mullins, C., 1992. Oriented and random sedimentation of plate-like clay particles in high centrifugal fields. J. Soild Sci. 43, 531–540.